DFT Study of deNO$_x$ Reactions in the Gas Phase: Mimicking the Reaction Mechanism over BaNaY Zeolites

Chun-Yi Sung, Randall Q. Snurr,* and Linda J. Broadbelt*

Institute for Catalysis in Energy Processes, Chemical and Biological Engineering Department, Northwestern University, 2145 Sheridan Road, Evanston, Illinois 60208

Received: December 10, 2008; Revised Manuscript Received: April 7, 2009

Neutral and ionic pathways for *aci*-nitromethane decomposition were studied in the gas phase, and the Gibbs free energy surfaces were constructed at 473 K. The pathways studied were based on proposed mechanisms of NO$_x$ reduction by acetaldehyde over BaNaY zeolites. Density functional theory at the B3LYP/6-311++G(d,p) level of theory was used, and 29 stable intermediates and 39 transition states were identified and quantified. Plausible pathways involving unimolecular decomposition or NO$_2$ addition were both explored. The rate constants for all elementary steps were estimated using transition state theory, and kinetic modeling was carried out to identify the dominant reaction channel. For the ionic routes, one of the NO$_2$ addition pathways dominated at typical NO$_2$ concentrations. For the neutral routes, one of the unimolecular decomposition routes was dominant. A solvation model was then included to mimic the environment of the BaNaY zeolite catalyst in a simplified manner. While inclusion of solvation effects stabilized the ionic species significantly, the dominant reaction channels in both the neutral and ionic systems were not altered. Our results show that the addition of NO$_2$ facilitates the decomposition of *aci*-anion nitromethane.

1. Introduction

Due to stricter air pollution standards that limit the permissible levels of toxic nitrogen oxides, NO and NO$_2$, in all industrialized countries, the catalysis community faces the challenge of designing a new catalyst that can selectively reduce NO$_x$ under lean-burn conditions where air is in excess, such as in diesel engines. Since Iwamoto discovered in the early 1990s that some zeolite-based catalysts are able to selectively carry out the reduction of NO$_x$ with hydrocarbons,[1,2] numerous catalysts have been studied for NO$_x$ reduction.[3−10] Among them, BaNaY zeolites with acetic acid or acetaldehyde as a reductant were recently found to be promising for NO$_x$ reduction because of their activity at relatively low temperatures (∼473 K) and their resistance to water vapor.[11−13]

Using FTIR spectroscopy and isotopic labeling, a plausible reaction mechanism for the reduction of NO$_x$ over BaNaY with acetic acid or acetaldehyde as a reductant was proposed by Yeom et al.[14] The essence of the proposed reaction mechanism is that acetate ions from acetaldehyde or acetic acid react with NO$_2$ to form nitromethane (NM), which decomposes to fulminic acid (HCNO) through a dinitromethane (DNM) intermediate. HCNO then isomerizes to isocyanic acid (HNCO), which then leads to the formation of N$_2$ via a mechanism that is well established.[14] Another plausible pathway is that nitromethane decomposes unimolecularly, which was proposed for the reaction of nitromethane over metal-exchanged zeolites by several groups.[15,16] Cowan et al. observed the facile reaction of nitromethane and NO$_2$ on Co-ZSM5, Na-ZSM5, and H-ZSM5, but with no well-established precedent for the direct reaction between NO$_2$ and adsorbed nitromethane, they proposed that nitromethane decomposes to HNCO and NH$_3$, which binds strongly and poisons the reaction sites. NO$_2$ then reacts with the bound NH$_3$ to give N$_2$. The unimolecular decomposition pathway was thought to be slower by Yeom et al., but no quantitative data was provided.

To elucidate how BaNaY zeolites catalyze deNO$_x$ reactions, it is useful to first study the reactions without the presence of the catalyst as a reference. The catalytic role of Ba in BaNaY zeolites can then be identified more clearly by comparison. In addition, the decomposition reactions of nitro-containing compounds are important for the significant role they play in propellant ignition, combustion, and atmospheric pollution.[17] In previous work,[18] we studied the adsorption properties of key reaction intermediates on the zeolitic barium cations using a hybrid quantum mechanical/molecular mechanical (QM/MM) method, with the ultimate goal of mapping transition states and the full reaction coordinate. As an intermediate step toward this goal, the comprehensive reaction mechanism is mapped in the gas phase in this paper. Because locating transition states on zeolites can be challenging, it is also hoped that the gas-phase calculations will provide guidance about which reaction pathways are the most dominant, as well as good initial guesses for calculations on the zeolite.

In a cation-exchanged zeolite environment, Yeom et al. postulated that intermediates dissociate into ions that are in equilibrium with their neutral counterparts, with the equilibrium constant dependent on the nature of the catalyst.[19] Therefore, we studied two sets of reaction pathways: all intermediates in their anionic form and in their neutral form. Three neutral pathways are studied in this work. Two of them, pathway 1 and pathway 2, involving unimolecular decomposition were also studied by Hu et al.,[20] and their results are compared with our results in section 3.1. Pathway 3 involves addition of NO$_2$ and was divided into three branches, pathways 3-1, 3-2, and 3-3. Three ionic pathways are also explored in section 3.2: pathway 1′ and pathway 2′ are the unimolecular routes, and pathway 3′ is the bimolecular route involving the addition of NO$_2$, which was again divided into three branches, pathways 3-1′, 3-2′, and 3-3′.

* Corresponding authors. E-mail: L.J.B., broadbelt@northwestern.edu; R.Q.S., snurr@northwestern.edu.

10.1021/jp810890m CCC: $40.75
Published on Web 05/21/2009

To mimic the environment in the zeolite in a very simplified way, we also studied these two sets of reaction pathways using a polarized continuum model (PCM)[21] with $CHCl_3$ as the solvent. $CHCl_3$ has a dielectric constant in the range of that imposed by cation-exchanged zeolites.[22] The Gibbs free energies of all stable intermediates and transition state structures were calculated at 473 K and compared. Transition state theory was employed to estimate the rate constants. Finally, kinetic modeling was carried out to quantify the relative contributions of the different reaction pathways under typical NO_x reduction conditions.

2. Computational Methods

All intermediates (IM) and transition state structures (TS) were optimized using density functional theory with the B3LYP level of theory and the 6-311++G(d,p) basis set. The 6-311++G(d,p) basis set, which is augmented with diffuse functions, has been specially designed for calculations involving anions.[23] The optimized transition state structures were confirmed as saddle points on the potential energy surface as characterized by one negative frequency, and intrinsic reaction coordinate (IRC) calculations were carried out to affirm that the transition state structures connect to the desired reactants and products. To include solvent effects, all the intermediates and transition state structures were also separately optimized with PCM. The molecular cavity around each solute was built by placing spheres around each atom with radii based on the UFF force field;[24] hydrogen atoms were explicitly defined. The solvent was set to $CHCl_3$, which has a dielectric constant of 4.9 that is close to that of sodium-exchanged 13X zeolites.[22] All ab initio calculations were carried out using Gaussian 03.[25]

Thermodynamic properties were calculated using standard statistical mechanical formulas within the rigid rotor, harmonic oscillator approximation. Selected calculations were carried out to assess the magnitude of internal rotation corrections within the one-dimensioned approximation.[26] The internal rotation corrections were small, with a maximum difference in Gibbs free energy of 0.76 kcal/mol, which was for the most complex molecule studied, hydrogenated dinitromethane. To calculate the vibrational contribution to the enthalpy and entropy, calculated frequencies were scaled by 0.9773 and 0.995, respectively. These values were based on a linear interpolation of the scale factors at 450 and 600 K recommended by Scott and Radom[27] for B3LYP/6-31G(d), which was the closest surrogate for the basis set that we employed. The Gibbs free energy was then obtained from the enthalpy and entropy in the standard way. Transition state theory was employed to estimate the rate constants via the standard expression including Wigner's tunneling correction:[28]

$$k = \Gamma(T) C_0^{\,1-n} \frac{k_b T}{h} e^{\frac{-\Delta G^{\ddagger}}{RT}} \tag{1}$$

with

$$\Gamma(T) = 1 + \frac{1}{24}\left(\frac{h|\nu^{\ddagger}|}{k_b T}\right)^2 \tag{2}$$

where C_0 is the concentration in the standard state to which the thermodynamic parameters are referred, i.e., P/RT, n is the molecularity of the reaction, k_b is Boltzmann's constant, h is Planck's constant, T is temperature, R is the ideal gas constant, $\Delta G^{\ddagger}$ is the difference between the Gibbs free energies of the transition state structure and the reactant, and $\nu^{\ddagger}$ is the imaginary frequency at the transition state.

Kinetic properties were obtained based on the TST rate constants via kinetic modeling. A simultaneous system of differential equations was constructed based on power law kinetics for each elementary step. Each one of the differential equations was formulated as

$$\begin{aligned}\frac{dC_i}{dt} = {} & \nu_{i1} k_1 [C_1]^{|\nu_{11}|}[C_2]^{|\nu_{21}|}\ldots[C_i]^{|\nu_{i1}|}\ldots + \\ & \nu_{i2} k_2 [C_1]^{|\nu_{12}|}[C_2]^{|\nu_{22}|}\ldots[C_i]^{|\nu_{i2}|}\ldots + \ldots \\ & \nu_{ij} k_j [C_1]^{|\nu_{1j}|}[C_2]^{|\nu_{2j}|}\ldots[C_i]^{|\nu_{ij}|}\ldots + \ldots\end{aligned} \tag{3}$$

where C_i is the concentration of species i, k_j is the rate constant for the jth elementary step, and ν_{ij} is the stoichiometric coefficient of species i in the jth elementary step. Concentrations of all species and rates of all elementary steps in a batch reactor were solved as a function of time. Initial concentrations of *aci*-NM and *aci*-anion NM were set to be 2.5×10^{-5} M, which is equivalent to 970 ppm. The initial concentration of NO_2 was varied as 2.5×10^{-7}, 2.5×10^{-6}, 2.5×10^{-5}, 2.5×10^{-4}, and 2.5×10^{-3} M to see its effect on HNCO or NCO^- generated and the relative rates of the different pathways.

3. Results and Discussion

3.1. Neutral Pathways. The proposed neutral reaction pathways are depicted in Figure 1. The first step involving NM is the isomerization to its aci form. Features of NM, including its structure, vibrational frequencies, and isomerization into its aci form, have been well studied experimentally and theoretically[17,29−35] because of its important role in combustion and atmospheric pollution. Therefore, the study of the isomerization step was not repeated. Only the staggered conformer of NM was calculated here, and its Gibbs free energy at 473 K was used as a reference for both the neutral and ionic pathways. The staggered conformer has been calculated to be more stable according to several studies,[31,35] and the rotation among the different conformers is nearly a free rotation, with a barrier of only 0.0061 kcal/mol.[29] The electronic energies and Gibbs free energies at 473 K of all intermediates and transition states are presented in Table 1. Figure 2 plots the free energy at 473 K for the neutral pathways. Structural details of all species are given in the Supporting Information. Details of the different pathways for the neutral intermediates are discussed in the following paragraphs.

pathway 1:

$$\textit{aci}\text{-NM} \xrightarrow{TS1} HCNO\ (IM1) + H_2O \xrightarrow{TS2} IM2 + H_2O \xrightarrow{TS3} HNCO + H_2O$$

aci-NM first undergoes a concerted water elimination via transition state (TS) TS1 as illustrated in Figure 1 and Figure 2. The activation barrier is 45.1 kcal/mol based on the electronic energy plus zero point energy and 44.0 kcal/mol for the Gibbs free energy. A transition state for this reaction was also found by Hu et al.[20] in their mapping of the potential energy surface for unimolecular decomposition of NM, and this route was

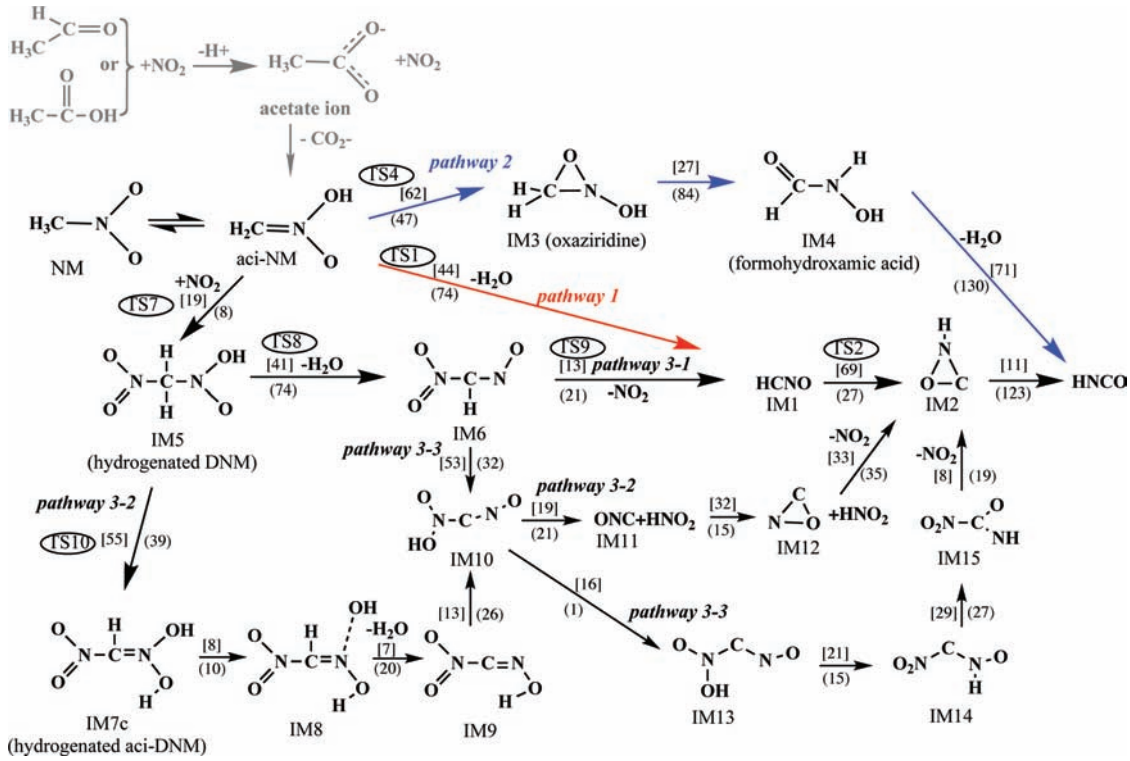

Figure 1. Neutral reaction pathways for forming HNCO from *aci*-NM. The forward and backward Gibbs free energy barriers are in square brackets and parentheses, respectively, in kcal/mol. Only selected transition states are labeled for simplification. Reactions prior to the formation of *aci*-NM were not studied computationally and are shown in gray.

TABLE 1: Relative Electronic Energies *E*, Electronic plus Zero Point Energies (ZPE) *E′*, Gibbs Free Energies *G* of Stable Intermediates (IM) and Transition State structures (TS), and Barrier Heights in Free Energy $\Delta G^{\ddagger}$ for Neutral Pathways at 473 K Calculated Using B3LYP/6-311++G(d,p)[a]

intermediates	*E*	*E′*	*G*	transition state structures	*E*	*E′*	*G*	$\Delta G^{\ddagger}$
NM + NO_2	0	0	0	TS1 + NO_2	63.6	58.6	58.9	44.0
aci-NM + NO_2	14.1	13.5	15.0	TS2 + H_2O + NO_2	75.0	68.3	53.8	69.2
IM1 + H_2O + NO_2	3.1	−2.17	−15.4	TS3 + H_2O + NO_2	60.0	52.9	38.1	10.7
IM2 + H_2O + NO_2	47.5	41.9	27.3	TS4 + NO_2	78.2	75.9	77.2	62.2
IM3 + NO_2	28.8	28.4	30.3	TS5 + NO_2	58.4	55.5	57.5	27.2
IM4 + NO_2	−27.4	−27.2	−26.0	TS6 + NO_2	50.4	44.5	45.2	71.2
IM5	4.8	7.31	26.2	TS7	16.3	16.7	34.4	19.4
IM6 + H_2O	−9.6	−10.9	−7.3	TS8	49.9	47.6	66.7	40.5
IM7c	20.4	22.0	42.1	TS9 + H_2O	8.12	4.06	5.7	12.9
IM8	25.2	24.9	40.5	TS10	61.4	60.4	81.4	55.2
IM9 + H_2O	26.2	24.5	27.6	TS11	29.9	30.4	50.5	8.4
IM10 + H_2O	15.6	13.0	14.3	TS12	35.6	31.3	48.0	7.5
IM11 + HNO_2 + H_2O	30.7	25.5	12.2	TS13 + H_2O	40.1	35.8	40.4	12.7
IM12 + HNO_2 + H_2O	50.9	44.5	29.3	TS14 + H_2O	35.5	31.8	33.3	18.9
IM13 + H_2O	28.6	26.4	29.7	TS15 + H_2O	66.6	59.7	44.6	32.4
IM14 + H_2O	35.5	33.4	36.0	TS16 + H_2O	69.0	61.1	62.7	33.4
IM15 + H_2O	35.9	34.1	37.7	TS17 + H_2O	47.3	42.6	46.1	53.4
HNCO + H_2O + NO_2	−66.3	−70.7	−84.7	TS18 + H_2O	28.8	26.3	30.6	16.2
				TS19 + H_2O	51.2	46.3	50.9	21.1
				TS20 + H_2O	65.1	61.6	65.1	29.2
				TS21 + H_2O	48.6	44.4	46.1	8.5

[a] Values are reported in kcal/mol. The structures of the intermediates are shown in Figure 1.

predicted to be the most feasible decomposition pathway for *aci*-NM. The electronic energy plus zero point energy barrier they calculated was 48.2 kcal/mol at the G2MP2 level of theory, which is in reasonably good agreement with our value. Next, isomerization steps between HCNO and HNCO were examined to complete this channel to form the final product. First, the hydrogen atom shifts to bond only to the nitrogen atom, while the oxygen atom migrates to the carbon atom, forming a CNO three-membered ring. This step was more energetically demandingly, with a free energy barrier of 69.2 kcal/mol. The second step, in which the NO bond is ruptured and the CNO three-membered ring opens, is more facile, with a free energy barrier of only 10.7 kcal/mol. The isomerization between HCNO and HNCO was also studied by Shapley et al.[36] at the Gaussian-2 level of theory. Our calculated electronic energy plus zero point energy barriers are 70.5 and 10.9 kcal/mol for the first and

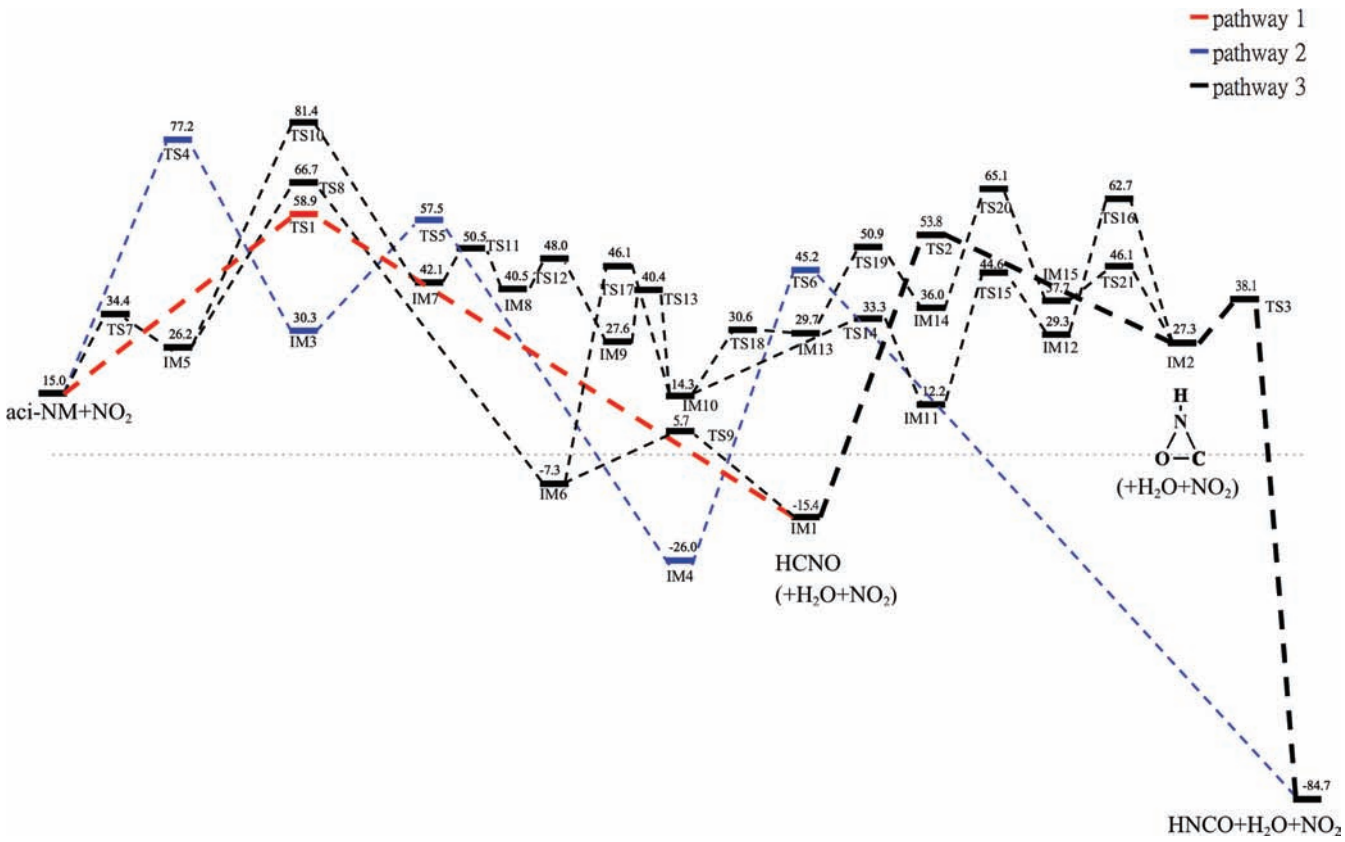

Figure 2. Gibbs free energy surface for neutral reaction pathways to form HNCO from *aci*-NM as shown in Figure 1 at 473 K. The dominant pathway, pathway 1, is delineated with a bold line. Structures of transition states in pathway 1 are shown in Figure 3.

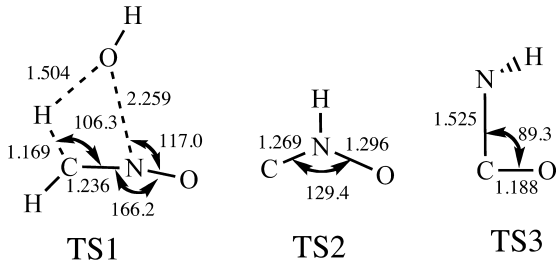

Figure 3. Structures of transition states in pathway 1. Bond lengths are in Å and angles in degrees.

second steps, respectively, which are in reasonable agreement with the barriers calculated by Shapley et al.: 67.4 and 14.2 kcal/mol.

pathway 2:

$$\textit{aci}\text{-NM} \xrightarrow{TS4} \text{oxaziridine (IM3)} \xrightarrow{TS5}$$

$$\text{formohydroxamic acid (IM4)} \xrightarrow{TS6} \text{HNCO} + \text{H}_2\text{O}$$

It was suggested by Cowan et al.[15] that *aci*-NM could isomerize to formohydroxamic acid (IM4) through a three-membered oxaziridine intermediate (IM3). We found transition states and stable intermediates composing this pathway. First, the non-hydroxyl oxygen atom migrated from the nitrogen atom to form a three-membered ring with both nitrogen and carbon. This step has an electronic energy plus zero point energy barrier of 62.4 kcal/mol. Hu et al.[20] also studied this step and found an electronic energy barrier of 61.3 kcal/mol, which is in very good agreement with our value. The CNO ring opens by transferring the oxygen atom further toward the carbon atom and transfers one hydrogen atom to the nitrogen atom to form the formohydroxamic acid intermediate (IM4). The electronic energy plus zero point energy barrier for this step was calculated to be 27.1 kcal/mol, which, surprisingly, is 24.0 kcal/mol lower than the corresponding barrier found by Hu et al.

The dehydration of formohydroxamic acid then leads directly to HNCO instead of having to pass through HCNO first as in the other paths. Cowan et al.[15] postulated that dehydration of formohydroxamic acid to HNCO should be easier than the dehydration of *aci*-NM to HCNO based on the relative weakness of the carbonyl CH bond. However, our results as well as those of Hu et al.[20] do not support this hypothesis. The dehydration of formohydroxamic acid was calculated to have an electronic and zero point energy barrier of 71.7 kcal/mol, which is 26.6 kcal/mol higher than that of pathway 1. This agrees well with the difference of 24.6 kcal/mol reported by Hu and co-workers.

pathway 3-1:

$$\textit{aci}\text{-NM} + \text{NO}_2 \xrightarrow{TS7} \text{hydrogenated DNM (IM5)} \xrightarrow{TS8}$$

$$\text{IM6} + \text{H}_2\text{O} \xrightarrow{TS9} \text{HCNO (IM1)} + \text{H}_2\text{O} + \text{NO}_2 \xrightarrow{TS2}$$

$$\text{IM2} + \text{H}_2\text{O} + \text{NO}_2 \xrightarrow{TS3} \text{HNCO} + \text{H}_2\text{O} + \text{NO}_2$$

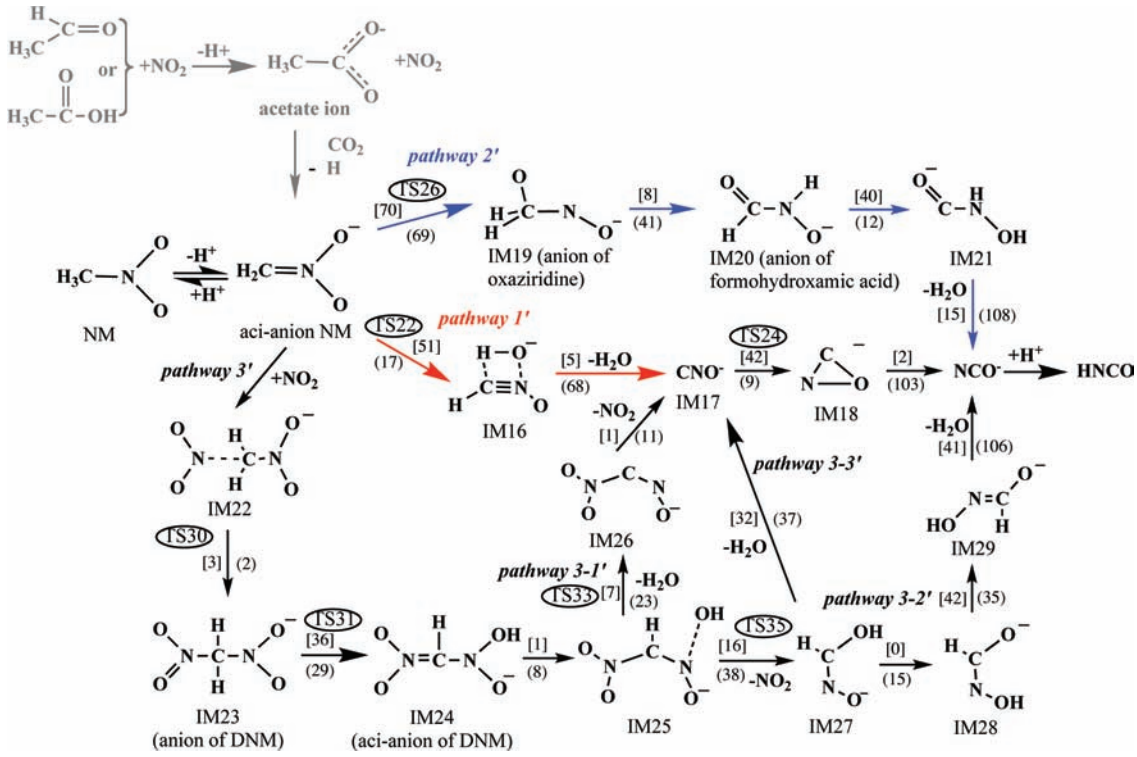

Figure 4. Ionic reaction pathways for forming NCO^- from *aci*-anion NM. The forward and backward Gibbs free energy barriers are in square brackets and parentheses, respectively, in kcal/mol. Only selected transition states are labeled for simplification. Reactions prior to the formation of *aci*-NM were not studied computationally and are shown in gray.

This alternative pathway is the neutral analogue of the ionic channel proposed by Yeom et al.[14] that starts with the addition of NO_2 to *aci*-anion NM. The neutral channel starts with the addition of NO_2 to *aci*-NM. The nitrogen atom of NO_2 adds to the carbon atom of *aci*-NM to give hydrogenated dinitromethane (DNM). The Gibbs free energy barrier for this addition step was calculated to be 19.4 kcal/mol. Hydrogenated DNM then undergoes water elimination to form O_2NCHNO (IM6) via TS8, in which a four-membered ring is formed by the linkage between the hydroxyl oxygen and one of the methylene hydrogen atoms. This step has a free energy barrier of 40.5 kcal/mol. IM6 then loses the nitro group to give HCNO via the fission of the CN bond in TS9, which has a small free energy barrier of 12.9 kcal/mol. HCNO can then isomerize to HNCO as in pathway 1.

pathway 3-2:

$$\textit{aci}\text{-NM} + NO_2 \xrightarrow{TS7} \text{hydrogenated DNM (IM5)} \xrightarrow{TS10}$$

$$\text{hydrogenated } \textit{aci}\text{-DNM (IM7c)} \xrightarrow{TS11} \text{IM8} \xrightarrow{TS12} \text{IM9} +$$

$$H_2O \xrightarrow{TS13} \text{IM10} + H_2O \xrightarrow{TS14} \text{CNO (IM11)} + HNO_2 +$$

$$H_2O \xrightarrow{TS15} \text{IM12} + HNO_2 + H_2O \xrightarrow{TS16}$$

$$\text{IM2} + NO_2 + H_2O$$

Another plausible route that Yeom et al.[14] considered (in ionic form) is for hydrogenated DNM to undergo an intramolecular hydrogen transfer to form hydrogenated *aci*-DNM (IM7). The neutral form presents complications not relevant to the ionic case because IM7 has two hydroxyl groups, which leads to twelve possibilities for hydrogen transfer and six different isomers of hydrogenated *aci*-DNM. All of the different possibilities were considered, and the comprehensive set of results is provided in the Supporting Information. The most feasible one is presented here as pathway 3−2.

The intramolecular hydrogen transfer of hydrogenated DNM to form hydrogenated *aci*-DNM involved a Gibbs free energy barrier of 55.2 kcal/mol, which is comparable to the barrier height of 52.2 kcal/mol estimated for DNM ⇌ *aci*-DNM by Khrapkovskii et al. at the B3LYP/6-311++G(d,p) level of theory.[37] A stable intermediate, IM8, with a loosely bound hydroxyl group is formed after breaking of the NO bond in IM7. Water is formed from the loose hydroxyl group and the methylene hydrogen and eliminated from IM8. After another intramolecular transfer for IM9 to form IM10, the CN bond breaks in TS14 to give HONO and linear CNO. After linear CNO transforms to bent CNO via TS15, it abstracts hydrogen from HONO through TS16 and affords IM2 and NO_2.

pathway 3-3:

$$\text{IM6} + H_2O \xrightarrow{TS17} \text{IM10} + H_2O \xrightarrow{TS18} \text{IM13} + H_2O \xrightarrow{TS19}$$

$$\text{IM14} + H_2O \xrightarrow{TS20} \text{IM15} + H_2O \xrightarrow{TS21}$$

$$\text{IM2} + H_2O + NO_2$$

Alternatively, IM6 can undergo intramolecular hydrogen transfer via TS17 to give IM10. IM10 isomerizes to IM13, which then undergoes another intramolecular hydrogen transfer to form an NH bond in IM14. An oxygen atom then migrates from

TABLE 2: Relative Electronic Energies *E*, Electronic Plus Zero Point Energies (ZPE) *E′*, Gibbs Free Energies *G* of Stable Intermediates (IM) and Transition State Structures (TS), and Barrier Heights in Free Energy $\Delta G^{\ddagger}$ for Ionic Pathways at 473 K Calculated Using B3LYP/6-311++G(d,p)[a]

intermediates	*E*	*E′*	*G*	transition state structures	*E*	*E′*	*G*	$\Delta G^{\ddagger}$
NM + NO_2	0	0	0	TS22 + NO_2	414.1	402.3	393.8	50.7
aci-anion NM + NO_2	360.9	352.1	343.1	TS23 + NO_2	405.9	393.3	382.0	5.0
IM16 + NO_2	395.3	386.1	377.1	TS24 + H_2O + NO_2	395.8	381.6	356.3	42.1
IM17 + H_2O + NO_2	349.2	337.3	314.2	TS25 + H_2O + NO_2	388.8	374.6	349.6	2.5
IM18 + H_2O + NO_2	386.3	372.5	347.1	TS26 + NO_2	432.7	422.1	413.3	70.2
IM19 + NO_2	363.5	353.7	344.0	TS27 + NO_2	373.6	361.1	352.4	8.4
IM20 + NO_2	329.2	320.9	311.8	TS28 + NO_2	372.6	360.6	351.6	39.7
IM21 + NO_2	358.2	348.8	339.3	TS29 + NO_2	374.6	363.6	353.9	14.6
IM22	339.3	331.7	339.3	TS30	340.9	334.2	341.8	2.6
IM23	335.6	330.1	339.4	TS31	374.5	365.8	375.6	36.2
IM24	346.7	340.0	347.8	TS32	346.8	339.7	348.9	1.1
IM25	343.1	335.1	340.5	TS33	349.7	340.6	347.2	6.7
IM26 + H_2O	342.3	332.4	324.5	TS34 + H_2O	344.7	333.5	325.0	0.5
IM27 + NO_2	337.1	328.1	319.2	TS35	365.4	353.5	356.9	16.4
IM28 + NO_2	321.0	312.9	304.0	TS36 + NO_2	337.2	327.1	318.8	−0.4
IM29 + NO_2	329.6	320.6	311.0	TS37 + NO_2	365.4	355.2	345.9	42.1
NCO^- + H_2O + NO_2	280.3	269.2	246.3	TS38 + NO_2	376.4	362.7	352.0	41.1
				TS39 + NO_2	378.4	366.1	351.4	32.2

[a] Values are reported in kcal/mol. The structures of the intermediates are shown in Figure 4.

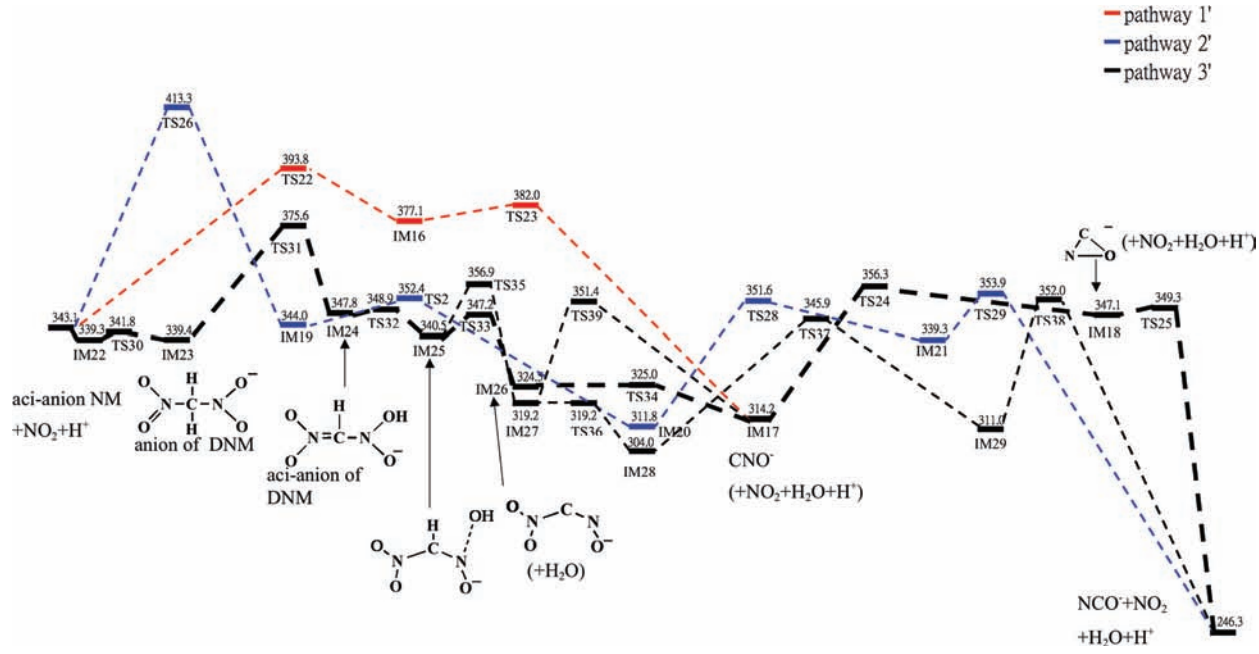

Figure 5. Gibbs free energy surface for ionic reaction pathways to form NCO^- from *aci*-anion NM as shown in Figure 4 at 473 K. The dominant pathway, pathway 3-1′, is delineated with a bold line. Structures of transition states in pathway 3-1′ are shown in Figure 6.

nitrogen to carbon via TS20 to give the HNCO moiety in IM15. Lastly, the nitro group leaves via NC bond fission in TS21 to give IM2.

3.2. Ionic Pathways. While the neutral pathways were studied with *aci*-NM as the starting point, the ionic pathways were explored with *aci*-anion NM as the starting point. The proposed reaction pathway is depicted in Figure 4. The electronic energies and Gibbs free energies at 473 K of all intermediates and transition states are listed in Table 2. The Gibbs free energy landscape at 473 K is also plotted in Figure 5. Structural details of all species are given in the Supporting Information. The calculated enthalpy and Gibbs free energy of *aci*-anion NM and a free proton at room temperature are 353.2 and 346.9 kcal/mol (not shown in Table 2) higher than those of NM, respectively. These energies are in reasonable agreement with the experimental values of the deprotonation enthalpies and Gibbs free energies of NM, which are 357.6 − 358.7 kcal/mol and 350.7 − 352.0 kcal/mol,[38,39] respectively.

pathway 1′:

$$\textit{aci}\text{-anion NM} \xrightarrow{TS22} \text{IM16} \xrightarrow{TS23} CNO^- \text{(IM17)} +$$

$$H_2O \xrightarrow{TS24} \text{IM18} + H_2O \xrightarrow{TS25} NCO^- + H_2O$$

Instead of a concerted water elimination as in pathway 1, a loosely bound hydroxyl group is first formed in IM16. Water is then formed from the hydroxyl group and the other hydrogen atom and eliminated from IM16 to give linear CNO^- (IM17).

The reaction then proceeds from linear CNO^- to NCO^- via a stable cyclic oxazirinyl anion intermediate. The free energy barriers for the last two steps are 42.1 and 2.5 kcal/mol, respectively. The rearrangement of the fulminate anion (CNO^-) to the cyanate anion (NCO^-) has been studied theoretically by other researchers at higher levels of theory such as CCSD(T) and MP2.[40−42] The electronic energy plus zero point energy barriers reported are 40.7−46.3 and 3.5−5.1 kcal/mol, respectively, which agree well with our calculated electronic energy plus zero point energy barriers, which were 44.3 and 2.1, respectively.

pathway 2′:

$$\textit{aci}\text{-anion NM} \xrightarrow{TS26} \text{anion of oxaziridine (IM19)} \xrightarrow{TS27}$$

$$\text{anion of formohydroxamic acid (IM20)} \xrightarrow{TS28}$$

$$\text{IM21} \xrightarrow{TS29} NCO^- + H_2O$$

Pathway 2′ mirrors pathway 2 except that the anion of formohydroxamic acid first transforms to IM21 with a hydroxyl group before water is formed and eliminated to give NCO^-. With the lengthened NO bond of 2.273 Å in the anion of oxaziridine (IM19), the CNO atoms are not considered to form a three-membered ring as they do in oxaziridine (IM3), which results in the structure of the anion of oxaziridine (IM19) more closely resembling the anion of formohydroxamic acid (IM20) than oxaziridine (IM3) resembles formohydroxamic acid (IM4). This increased similarity results in a free energy barrier of 8.4 kcal/mol for the transition of the anion of oxaziridine (IM19) to the anion of formohydroxamic acid (IM20), which is much lower than that for forming formohydroxamic acid (IM4) from oxaziridine (IM3), 27.2 kcal/mol.

pathway 3-1′:

$$\textit{aci}\text{-anion NM} + NO_2 \rightarrow \text{IM22} \xrightarrow{TS30}$$

$$\text{anion of DNM (IM23)} \xrightarrow{TS31} \textit{aci}\text{-anion DNM (IM24)} \xrightarrow{TS32}$$

$$\text{IM25} \xrightarrow{TS33} \text{IM26} + H_2O \xrightarrow{TS34} CNO^- \text{(IM17)} + H_2O \xrightarrow{TS24}$$

$$\text{IM18} + H_2O \xrightarrow{TS25} NCO^- + H_2O + NO_2$$

This pathway was explored based on the ionic pathway involving NO_2 that was first proposed by Yeom et al.[14] The corresponding neutral pathway is pathway 3-2; however, there are two more intermediates in this ionic pathway: (1) a precursor for the addition of NO_2 to *aci*-anion NM (IM22), and (2) a precursor for water elimination (IM25). In IM22, the nitro group is stabilized in the vicinity of *aci*-anion NM. In IM25, the hydroxyl group becomes loosely bound via TS32, which only has a barrier height of 1 kcal/mol in free energy for the NO bond rupture.

pathway 3-2′:

$$\text{IM25} \xrightarrow{TS35} \text{IM27} + NO_2 \xrightarrow{TS36} \text{IM28} +$$

$$NO_2 \xrightarrow{TS37} \text{IM29} + NO_2 \xrightarrow{TS38} NCO^- + H_2O + NO_2$$

In contrast to water elimination followed by nitro group elimination in pathway 3-1′, an alternative is that the nitro group is eliminated first, followed by water elimination, which is labeled pathway 3-2′. Another difference is that the barrierless isomerization from IM27 to IM28 leads to the formation of IM29, which is well positioned to lead to NCO^- directly as the final product after water elimination, without having to pass through CNO^-.

pathway 3-3′:

$$\text{IM27} + H_2O \xrightarrow{TS39} CNO^- \text{(IM17)} + H_2O \xrightarrow{TS24}$$

$$\text{IM18} + H_2O \xrightarrow{TS25} NCO^- + H_2O + NO_2$$

An additional branch emanating from pathway 3-2′ is when IM27 loses water and gives CNO^-, which is designated as pathway 3-3′. CNO^- (IM17) then follows the same route as pathway 3-1′ to form the final product, NCO^-.

3.3. Solvent Effect. The effect of a dielectric continuum on the energetics of the neutral and ionic pathways is tabulated in Table 3. The differences in the free energy barrier heights and reaction free energies between the gas phase and in the presence of a solvent range from −8.2 to +5.2 kcal/mol and −11.3 to +6.1 kcal/mol, respectively, without an obvious trend. The free energies of the ionic species in solvent (both stable intermediates and transition state structures) are lowered by more than 30 kcal/mol from those in the gas phase. This indicates that the ionic species are stabilized significantly by solvent, as expected. However, the free energies of reaction and the free energy barriers are not changed significantly by the solvent effect.

3.4. Kinetic Modeling. The rate constants for all of the elementary steps that were estimated from eq 1 and used in kinetic modeling are listed in Tables S1 and S2 in the Supporting Information. For both the neutral and the ionic chemistry, the dominant pathways leading to the formation of HNCO were determined from the net rates calculated using kinetic modeling. The net rate analysis was performed with the initial NO_2 concentration varied from 2.5×10^{-7} to 2.5×10^{-3} M. Interestingly, our results showed that the dominant pathway for HNCO formation is different for the neutral and ionic cases. Furthermore, the inclusion of solvent effects via PCM does not alter the dominant neutral and ionic pathways. Pathway 1 is dominant in the neutral case, with greater than 99% of the flux. This conclusion was insensitive to the NO_2 concentration used, indicating that the bimolecular pathway is never competitive for the reasonable range of NO_2 concentrations explored. While the addition of NO_2 to *aci*-nitromethane has the lowest free energy barrier, hydrogenated dinitromethane (IM5) is thermodynamically uphill from *aci*-nitromethane and NO_2 (Figure 2). In contrast, the loss of water from *aci*-nitromethane to form HCNO (IM1) is thermodynamically downhill. The further reaction of hydrogenated dinitromethane (IM5) requires surmounting a free energy barrier of 55.2 kcal/mol and presents a

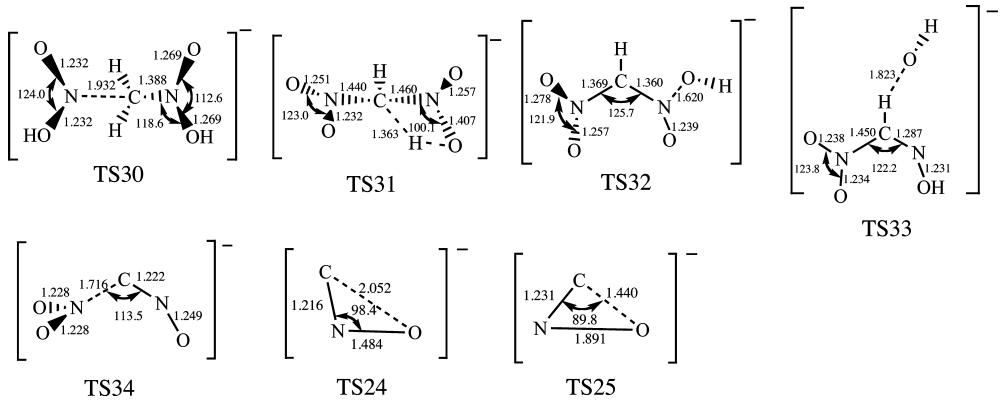

Figure 6. Structures of transition states in pathway 3-1′. Bond lengths are in Å and angles in degrees.

TABLE 3: Relative Electronic Energies *E*, Gibbs Free Energies *G* of Stable Intermediates (IM) and Transition State Structures (TS), Change of Barrier Heights in Free Energies $\Delta(\Delta G^{\ddagger})$ in $CHCl_3$ Compared to the Gas Phase, and Change of Reaction Free Energies $\Delta(\Delta G_R)$ in $CHCl_3$ Compared to the Gas Phase at 473 K Calculated at B3LYP/6-311++G(d,p)[a]

intermediates	*E*	*G*	transition state structures	*E*	*G*	ΔG	$\Delta(\Delta G^{\ddagger})$	$\Delta(\Delta G_R)$
NM + NO_2	0	0	TS1 + NO_2	62.4	57.8	42.7	−1.3	2.14
aci-NM + NO_2	14.6	15.0	TS2 + H_2O + NO_2	69.7	47.8	61.0	−8.2	−4.53
IM1 + H_2O + NO_2	0.9	−13.2	TS3 + H_2O + NO_2	59.7	37.0	12.0	1.3	−0.45
IM2 + H_2O + NO_2	46.0	25.1	TS4 + NO_2	74.3	73.5	58.4	−3.8	−0.10
IM3 + NO_2	28.9	30.3	TS5 + NO_2	52.7	52.2	21.9	−5.3	−1.92
IM4 + NO_2	−29.0	−28.0	TS6 + NO_2	50.2	44.6	72.5	1.3	−0.83
IM5	3.1	24.4	TS7	16.5	34.2	19.1	−0.3	−1.90
IM6 + H_2O	−12.1	−10.9	TS8	48.3	65.0	40.6	0.1	−1.84
IM7c	15.9	37.7	TS9 + H_2O	6.5	3.2	14.1	1.2	5.87
IM8	24.6	40.0	TS10	60.4	80.1	55.6	0.4	−2.62
IM9 + H_2O	23.8	24.4	TS11	28.9	49.3	11.6	3.2	3.89
IM10 + H_2O	12.3	8.6	TS12	34.8	48.4	8.4	0.9	−2.75
IM11 + HNO_2 + H_2O	28.9	9.8	TS13 + H_2O	37.9	37.4	13.0	0.3	−2.50
IM12 + HNO_2 + H_2O	49.4	27.1	TS14 + H_2O	33.5	30.6	22.1	3.2	3.39
IM13 + H_2O	25.9	26.0	TS15 + H_2O	65.4	42.6	32.8	0.4	0.16
IM14 + H_2O	31.0	31.3	TS16 + H_2O	68.6	61.6	34.5	1.1	−0.06
IM15 + H_2O	32.3	33.1	TS17 + H_2O	46.3	44.2	55.1	1.7	−1.85
HNCO + H_2O + NO_2	−68.1	−87.4	TS18 + H_2O	25.9	26.8	17.9	1.7	1.79
			TS19 + H_2O	48.5	47.3	21.3	0.1	−1.02
			TS20 + H_2O	60.4	59.9	28.6	−0.6	0.14
			TS21 + H_2O	48.0	44.1	11.0	2.5	2.28
NM + NO_2	0	0	TS22 + NO_2	370.5	350.2	52.9	2.2	1.31
aci-anion NM + NO_2	314.7	297.3	TS23 + NO_2	357.9	336.5	4.0	−1.0	−4.58
IM16 + NO_2	350.8	332.5	TS24 + H_2O + NO_2	345.8	305.6	40.5	−1.6	−1.21
IM17 + H_2O + NO_2	300.9	265.1	TS25 + H_2O + NO_2	339.6	299.3	2.5	0.0	−0.82
IM18 + H_2O + NO_2	336.8	296.8	TS26 + NO_2	382.4	363.2	66.0	−4.2	1.20
IM19 + NO_2	318.4	299.4	TS27 + NO_2	330.1	309.2	9.8	1.4	−2.62
IM20 + NO_2	281.7	264.6	TS28 + NO_2	328.3	307.3	42.7	3.0	3.12
IM21 + NO_2	314.2	295.2	TS29	331.7	311.0	15.8	1.2	−7.0
IM23	294.5	298.4	TS31	336.0	337.2	38.8	2.6	−1.01
IM24	303.6	305.8	TS32	307.8	309.6	3.8	2.7	6.07
IM25	306.2	304.6	TS33	311.2	310.7	6.1	−0.6	−5.05
IM26 + H_2O	302.2	283.6	TS34 + H_2O	305.3	284.4	0.9	0.4	−8.13
IM27 + NO_2	289.3	272.0	TS35	331.9	322.6	18.1	1.7	−11.3
IM28 + NO_2	275.6	258.6	TS36 + NO_2	289.8	271.2	−0.7	−0.3	1.82
IM29 + NO_2	282.0	263.6	TS37 + NO_2	319.1	300.0	41.3	−0.8	−1.94
NCO^{-1} + H_2O + NO_2	229.9	195.1	TS38 + NO_2	333.4	309.8	46.3	5.2	−3.74
			TS39 + NO_2	332.4	309.2	37.3	5.1	−1.84

[a] Values are reported in kcal/mol.

bottleneck, and thus the dominant flux of the reaction of *aci*-nitromethane proceeds via pathway 1. As shown in Figure 7, the net rate of the decomposition of *aci*-NM through pathway 3 (TS7) increases with the initial NO_2 concentration. However, pathway 1 remains dominant within the range in which the initial NO_2 concentration was varied.

While the final product, HNCO, was sought, only a negligible amount was formed on the time scale studied (up to 2.5×10^4 h). Instead, the precursor to HNCO, HCNO, was formed in high yields. As illustrated in Figure 2, HCNO + H_2O is thermodynamically downhill from *aci*-nitromethane, and thus its formation is favorable. However, conversion of HCNO to HNCO requires surmounting a free energy barrier of 69.2 kcal/mol, which is prohibitive at the conditions studied. Although formohydroxamic acid (IM4) is the intermediate with the lowest free energy along the reaction coordinate, its formation demands

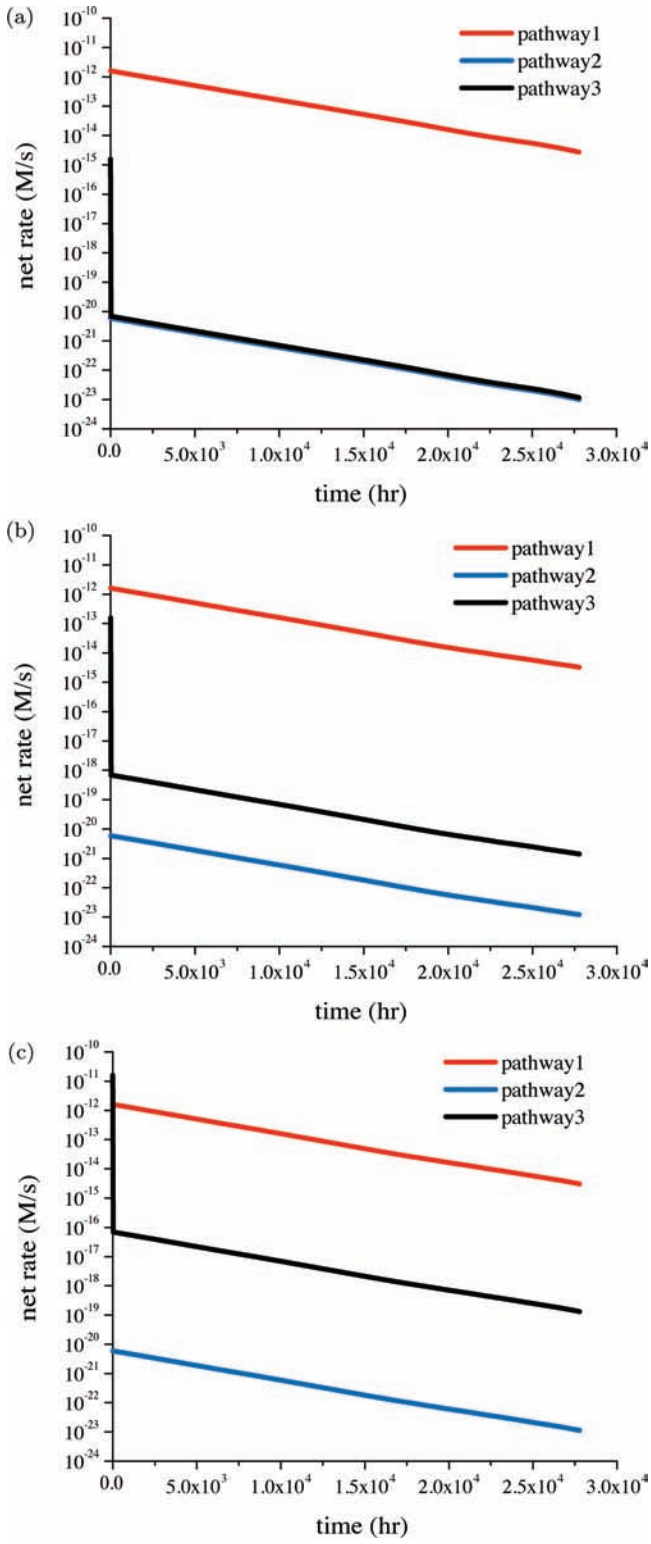

Figure 7. Net rates (on logarithmic scale) of decomposition of *aci*-NM through pathways 1, 2, and 3 (via TS1, TS4, and TS7, respectively) with the initial NO_2 concentrations set as (a) 2.5×10^{-7} M, (b) 2.5×10^{-5} M, and (c) 2.5×10^{-3} M.

overcoming a free energy barrier of 62.2 kcal/mol associated with TS4, which renders it infeasible. Thus, pathway 2 is never competitive at the conditions examined.

The results of the kinetic analysis reveal that the dominant pathway for the ionic chemistry is pathway 3-1′, with a relative rate over 99% for all NO_2 concentrations examined. Pathway 1′ is never competitive as the barrier for unimolecular conversion of *aci*-anion NM to IM16 is 51 kcal/mol, which is higher than all the barriers along pathway 3-1′, and IM16 is thermodynamically uphill on the free energy surface compared to all intermediates and transition states along all the other pathways (Figure 5). Pathway 2′ demands overcoming an even higher free energy barrier (70 kcal/mol) than pathway 1′, and thus the unimolecular decomposition of *aci*-anion NM to form the anion oxaziridine (IM19) has a negligible rate. The addition of NO_2 to *aci*-anion NM is so facile that the NO_2 concentration would have to be lowered to a value of 5.0×10^{-11} M before either of the unimolecular decomposition pathways competes successfully. Pathways 3-2′ and 3-3′ diverge from pathway 3-1′ at IM25. Pathways 3-2′ and 3-3′ involve the loss of NO_2 from IM25 with a free energy barrier of 16 kcal/mol, while pathway 3-1′ involves the more facile loss of H_2O from IM25 with a free energy barrier of 7 kcal/mol. Thus, the majority of the flux passes through pathway 3-1′ to form CNO^-, which accumulates initially and then rearranges to form NCO^-.

4. Conclusion

The decomposition pathways for *aci*-NM to HNCO and for *aci*-anion NM to NCO^- were investigated in the gas phase at the B3LYP/6-311++G(d,p) theory of level. For both systems, two categories of reaction pathways were involved: unimolecular decomposition pathways and NO_2 addition pathways. The Gibbs free energy surfaces at 473 K for neutral and ionic pathways were established, and rate constants were estimated from free energy barriers using transition state theory including Wigner's tunneling correction. Our kinetic modeling showed that one of the NO_2 addition pathways is dominant among the ionic pathways (pathway 3-1′), whereas one of the unimolecular decomposition pathways is dominant among the neutral pathways (pathway 1). The inclusion of solvent effects with the polarized continuum model stabilizes ionic species significantly, but the dominant pathways are not altered from the gas-phase results. Our results suggest that the addition of NO_2 does facilitate the decomposition of *aci*-anion NM.

Acknowledgment. This work was supported by the Chemical Sciences, Geosciences, and Biosciences Division, Office of Basic Energy Sciences, Office of Science, U.S. Department of Energy Grant No. DE-FG02-03ER15457. This research used resources of the National Energy Research Scientific Computing Center, which is supported by the Office of Science of the U.S. Department of Energy under Contract No. DE-AC02-05CH11231.

Supporting Information Available: Hydrogenated DNM (IM5) could undergo an intramolecular hydrogen transfer to form six isomers of hydrogenated *aci*-DNM (IM7), which might decompose via different routes. All of the relevant routes are discussed in section 1. Structural details of all stable intermediates and transition states are given in section 2. The rate constants for all of the elementary steps are listed in Tables S1 and S2 in section 3. This material is available free of charge via the Internet at http://pubs.acs.org.

References and Notes

(1) Iwamoto, M.; Yahiro, H.; Tanda, K.; Mizuno, N.; Mine, Y.; Kagawa, S. *J. Phys. Chem.* **1991**, *95*, 3727–3730.
(2) Iwamoto, M.; Yahiro, H.; Shundo, S.; Yoshihiro, Y.; Mizuno, N. *Appl. Catal.* **1991**, *69*, L15–L19.
(3) Amiridis, M. D.; Zhang, T. J.; Farrauto, R. J. *Appl. Catal., B* **1996**, *10*, 203–227.
(4) Shelef, M. *Chem. Rev.* **1995**, *95*, 209–225.
(5) Armor, J. *Catal. Today* **1995**, *26*, 147–158.

(6) Campa, M. C.; Pietrogiacomi, D.; Tuti, S.; Ferraris, G.; Indovina, V. *Appl. Catal., B* **1998**, *18*, 151–162.
(7) Oleksenko, L. P.; Yatsimirsky, V. K.; Telbiz, G. M.; Lutsenko, L. V. *Adsorpt. Sci. Technol.* **2004**, *22*, 535–541.
(8) Tabata, T.; Kokitsu, M.; Okada, O. *Catal. Lett.* **1994**, *25*, 393–400.
(9) Adelman, B. J.; Sachtler, W. M. H. *Appl. Catal., B* **1997**, *14*, 1–11.
(10) Chen, H. Y.; Sachtler, W. M. H. *Catal. Today* **1998**, *42*, 73–83.
(11) Kwak, J. H.; Szanyi, J.; Peden, C. *J. Catal.* **2003**, *220*, 291–298.
(12) Kwak, J. H.; Szanyi, J.; Peden, C. *Catal. Today* **2004**, *89*, 135–141.
(13) Chen, H. Y.; Sun, Q.; Wen, B.; Yeom, Y. H.; Weitz, E.; Sachtler, W. M. H. *Catal. Today* **2004**, *96*, 1–10.
(14) Yeom, Y. H.; Wen, B.; Sachtler, W. M. H.; Weitz, E. *J. Phys. Chem. B* **2004**, *108*, 5386–5404.
(15) Cowan, A. D.; Cant, N. W.; Haynes, B. S.; Nelson, P. F. *J. Catal.* **1998**, *176*, 329–343.
(16) Blower, C. J.; Smith, T. D. *Zeolites* **1993**, *13*, 394–398.
(17) McKee, M. L. *J. Am. Chem. Soc.* **1986**, *108*, 5784–5792.
(18) Sung, C.-Y.; Broadbelt, L. J.; Snurr, R. Q. *Catal. Today* **2008**, *136*, 64–75.
(19) Yeom, Y. H.; Li, M.; Savara, A.; Sachtler, W. M. H.; Weitz, E. *Catal. Today* **2008**, *136*, 55–63.
(20) Hu, W. F.; He, T. J.; Chen, D. M.; Liu, F. C. *J. Phys. Chem. A* **2002**, *106*, 7294–7303.
(21) Cancés, E.; Mennucci, B.; Tomasi, J. *J. Chem. Phys.* **1997**, *107*, 3032041.
(22) Thiebaut, J. M.; Akyel, C.; Roussy, G.; Bosiso, R. G. *IEEE Trans. Instrum. Meas.* **1988**, *37*, 114–120.
(23) Spitznagel, G. W.; Clark, T.; Chandrasekhar, J.; Schleyer, P. V. *J. Comput. Chem.* **1988**, *3*, 363–371.
(24) Rappé, A. K.; Casewit, C. J.; Colwell, K. S.; Goddard, W. A.; Skiff, W. M. *J. Am. Chem. Soc.* **1992**, *114*, 10024–10035.
(25) Frisch, M. J.; Trucks, G. W.; Schlegel, H. B.; Scuseria, G. E.; Robb, M. A.; Cheeseman, J. R.; Montgomery, J. A., Jr.; Vreven, T.; Kudin, K. N.; Burant, J. C.; Millam, J. M.; Iyengar, S. S.; Tomasi, J.; Barone, V.; Mennucci, B.; Cossi, M.; Scalmani, G.; Rega, N.; Petersson, G. A.; Nakatsuji, H.; Hada, M.; Ehara, M.; Toyota, K.; Fukuda, R.; Hasegawa, J.; Ishida, M.; Nakajima, T.; Honda, Y.; Kitao, O.; Nakai, H.; Klene, M.; Li, X.; Knox, J. E.; Hratchian, H. P.; Cross, J. B.; Bakken, V.; Adamo, C.; Jaramillo, J.; Gomperts, R.; Stratmann, R. E.; Yazyev, O.; Austin, A. J. ; Cammi, R.; Pomelli, C.; Ochterski, J. W.; Ayala, P. Y.; Morokuma, K.; Voth, G. A.; Salvador, P.; Dannenberg, J. J.; Zakrzewski, V. G.; Dapprich, S.; Daniels, A. D.; Strain, M. C.; Farkas, O.; Malick, D. K.; Rabuck, A. D.; Raghavachari, K.; Foresman, J. B.; Ortiz, J. V.; Cui, Q.; Baboul, A. G.; Clifford, S.; Cioslowski, J.; Stefanov, B. B.; Liu, G.; Liashenko, A.; Piskorz, P.; Komaromi, I.; Martin, R. L.; Fox, D. J.; Keith, T.; Al-Laham, M. A.; Peng, C. Y.; Nanayakkara, A.; Challacombe, M.; Gill, P. M. W.; Johnson, B.; Chen, W.; Wong, M. W.; Gonzalez, C.; Pople, J. A. *Gaussian 03, Revision D.02*; Gaussian, Inc.: Wallingford, CT, 2004.
(26) Pfaendtner, J.; Yu, X.; Broadbelt, L. J. *Theor. Chem. Acc.* **2007**, *118*, 881–898.
(27) Scott, A. P.; Radom, L. *J. Phys. Chem.* **1996**, *100*, 16502–16513.
(28) Hirschfelder, J. O.; Wigner, E. *J. Chem. Phys.* **1939**, *7*, 616–628.
(29) Cox, A. P.; Waring, S. *J. Chem. Soc., Faraday Trans. 2* **1971**, *68*, 1060–1071.
(30) Murrell, J. N.; Vidal, B.; Guest, M. F. *J. Chem. Soc., Faraday Trans. 2* **1975**, *71*, 1577–1582.
(31) McKee, M. L. *J. Am. Chem. Soc.* **1985**, *107*, 1900–1904.
(32) Lammertsma, K.; Prasad, B. V. *J. Am. Chem. Soc.* **1993**, *115*, 2348–2351.
(33) Allouche, A. *J. Phys. Chem.* **1996**, *100*, 1820–1826.
(34) Tokmakov, I. V.; Shlyapochnikov, V. A. *Russ. Chem. Bull.* **1997**, *46*, 1992–1995.
(35) Gorse, D.; Cavagnat, D.; Pesquer, M.; Lapouge, C. *J. Phys. Chem.* **1993**, *97*, 4262–4269.
(36) Shapley, W. A.; Bacskay, G. B. *J. Phys. Chem. A* **1999**, *103*, 6624–6631.
(37) Khrapkovskii, G. M.; Shamov, A. G.; Shamov, G. A.; Shlyapochnikov, V. A. *Russ. Chem. Bull.* **2001**, *50*, 952–957.
(38) Bartmess, J. E.; Scott, J. A.; Mciver, R. T. *J. Am. Chem. Soc.* **1979**, *101*, 6046–6056.
(39) Cumming, J. B.; Kebarle, P. *Can. J. Chem.* **1978**, *56*, 1–9.
(40) Li, W. K.; Baker, J.; Radom, L. *Aust. J. Chem.* **1986**, *39*, 913–921.
(41) Pak, Y.; Woods, R. C.; Peterson, K. A. *J. Chem. Phys.* **1997**, *106*, 5123–5132.
(42) Dua, S.; Bowie, J. H. *J. Phys. Chem. A* **2003**, *107*, 76–82.

JP810890M